POLITECNICO DI TORINO
Repository ISTITUZIONALE

Collective migration and patterning during early development of zebrafish posterior lateral line

(Article begins on next page)

25 April 2024

Author for correspondence:
Annachiara Colombi
e-mail: annachiara.colombi@polito.it

Collective migration and patterning during early development of zebrafish posterior lateral line

Annachiara Colombi, Marco Scianna and Luigi Preziosi

Department of Mathematical Sciences, Politecnico di Torino, Corso Duca degli Abruzzi 24, 10129 Torino, Italy

AC, 0000-0001-6282-3326; MS, 0000-0003-3509-9015; LP, 0000-0003-1532-1854

The morphogenesis of zebrafish posterior lateral line (PLL) is a good predictive model largely used in biology to study cell coordinated reorganization and collective migration regulating pathologies and human embryonic processes. PLL development involves the formation of a placode formed by epithelial cells with mesenchymal characteristics which migrates within the animal myoseptum while cyclically assembling and depositing rosette-like clusters (progenitors of neuromast structures). The overall process mainly relies on the activity of specific diffusive chemicals, which trigger collective directional migration and patterning. Cell proliferation and cascade of phenotypic transitions play a fundamental role as well. The investigation on the mechanisms regulating such a complex morphogenesis has become a research topic, in the last decades, also for the mathematical community. In this respect, we present a multiscale hybrid model integrating a discrete approach for the cellular level and a continuous description for the molecular scale. The resulting numerical simulations are then able to reproduce both the evolution of *wild-type* (i.e. normal) embryos and the pathological behaviour resulting form experimental manipulations involving laser ablation. A qualitative analysis of the dependence of these model outcomes from cell-cell mutual interactions, cell chemical sensitivity and internalization rates is included. The aim is first to validate the model, as well as the estimated parameter values, and then to predict what happens in situations not tested yet experimentally.

This article is part of the theme issue 'Multi-scale analysis and modelling of collective migration in biological systems'.

1. Introduction

The *lateral line* is a sensory system present in fishes and amphibians which, detecting water displacements, is involved in fundamental activities such as prey and predator detection, obstacle avoidance, collective swimming and courtship [1,2]. It consists of a set of mechanosensory organs, named *neuromasts*, arranged in a species-specific pattern over the surface of the body, connected to the brain by a network of afferent neurons [1]. In particular, the *posterior lateral line* (PLL) is the portion located over the trunk and tail of the animal [1].

In the last decades, the development of PLL in *zebrafish* embryos has been widely employed as a good predictive model to shed light on the main biophysical mechanisms at the basis of the *collective* and *coordinated* cell organization and migration characterizing both physiological (e.g. organogenesis or wound healing) and pathological situations (e.g. tumour growth or the Duchenne muscolar dystrophy), see [3–6] and references therein. In particular, the large experimental use of this highly fecund small tropical fish is mainly owing to the fact that (i) it has almost 70% of human genes, (ii) its embryos are transparent and (iii) rapidly develop outside its body (in about 24–48 h after fertilization).

The embryonic development of the zebrafish PLL begins around 19 h post egg fertilization (hpf) with the formation of a small placode of about 100 epithelial cells (with mesenchymal characteristics), named *primordium* (PLLp), located in the horizontal myoseptum just caudal to the otic vesicle, see figure 1*a* [2,7]. Then different phases can be identified. Over the next 24–30 h, the primordium
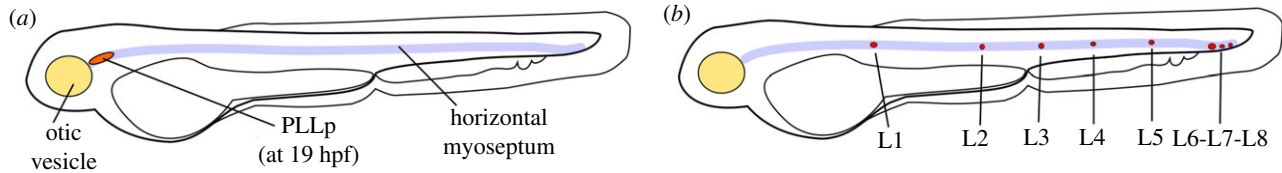
Figure 1. Sketches of posterior lateral line (PLL) appearance at the beginning (*a*) and the end (*b*) of zebrafish embryonic growth. (*a*) Zebrafish PLL arises around 19 h post egg fertilization (hpf) as an epithelial placode (orange ellipse), said primordium, located in the horizontal myoseptum (blue line) just caudal to the otic vesicle (yellow circle). (*b*) Typical pattern of proto-neuromasts (red dots), named L1-L8, constituting zebrafish PLL at the end of its embryonic growth, i.e. about 24–30 h after the formation of the primordium. (Online version in colour.)

migrates towards the tail of the animal while depositing at given time instants and distances, seven to eight neuromast progenitors, termed *proto-neuromasts* or *rosettes* (owing to their characteristic shape), as sketched in figure 1*b*, (see the dots named L1-L8). Trails of interneuromastic cells are possibly located between consecutive rosettes. Successively, during zebrafish post-embryonic growth, cells within each proto-neuromast acquire either a hair or a supporting fate, giving rise to a fully developed neuromast. To complete the PLL system, additional mechanosensory organs are provided by interneuromastic cell proliferation and the development of secondary additional primordia. Finally, a mature neuronal network organizes and extends for brain connection.

The early stage of the zebrafish PLL formation is here studied with a hybrid and multiscale mathematical framework, that couples different modelling techniques (i.e. discrete versus continuous), each of them in turn dealing with a different scale (i.e. subcellular versus cellular). The proposed approach is able to reproduce *in silico* both the physiological development of embryonic PLL and selected experimental manipulations based on laser ablation of the migrating primordium. A series of numerical simulations will both highlight how the proposed model outcomes depend on selected parameters, and provide *in silico* predictions of the evolution of PLL primordium upon the increase/decrease of either cell-cell interactions, or cell chemical sensitivity and internalization rates.

Terminological remark. For the reader's convenience, we here clarify the terminology adopted in the rest of the manuscript. The terms 'proto-neuromast' and 'rosette' will be used as synonymous. Cells will be also denoted as 'agents', 'individuals' or 'points'. Two chemicals regulating the development of zebrafish PLL will be considered: the fibroblast growth factor 10a, hereafter FGF10, (fgf10a in Zebrafish Information Network, ZFIN); and the stromal cell-derived factor 1, here called SDF1a (cxcl12a in ZFIN). Cell response to these chemicals will be, respectively, mediated by the fibroblast growth factor receptor 1a, hereafter *fgfr1* (fgfr1a in ZFIN); and one SDF1a receptor between the chemokine (C-X-C motif) receptor of 4b, here named *Cxcr4* (cxcr4b in ZFIN), and the atypical chemokine receptor 3b, here called *Cxcr7* (ackr3b in ZFIN). Finally, bold script will be used to indicate vectorial quantities, normal script for scalar ones, and italic script for neighbourhoods.

2. Biological and modelling background

In this section, we first summarize the main mechanisms underlying the processes of interest, that are inferred by a scan of the experimental literature, referring in particular to [1,2,5,7–19], and that will constitute the simplified assumptions at the basis of the proposed mathematical model. Then,

we will outline the modelling literature specifically focusing on the early development of zebrafish PLL.

(a) Biological background
(i) Cell and molecular levels

The initial state of the cells forming the primordium is *pseudo-mesenchymal* (PM). In fact, regardless of their epithelial genotype, they display high levels of motility and low levels of adhesiveness. Moreover, PM cells produce chemical fibroblast growth factor 10 (FGF10), while expressing the stromal-derived factor 1a (SDF1a) migratory-related receptor *Cxcr4*. PM individuals, as well as maintaining their state, may undergo two distinct fates, see figure 2*a*. Few of them singularly *activate* (and are denoted by 'aPM'), becoming the centre of the rosette-like structures that progressively form and mature (see later). aPMs are observed to maintain high levels of motility and the basal level of FGF10 secretion and of *Cxcr4* expression, while increasing their adhesive ability.

Each aPM then induces a phenotypic transition of a cluster of nearly 25 PM cells in its surroundings, which will form the body of a rosette. These *deactivated pseudo-mesenchymal* individuals (identified by 'dPM') are no longer able to produce FGF10; rather they start to express its receptor *fgfr1*, being thereby chemotactically attracted towards detected higher amounts of FGF10. dPM cells are irreversibly characterized by two further state changes. First, they undergo a partial epithelialization (and are labelled by 'pE', *partially epithelial*), which involves the expression of non-migratory-related SDF1a receptor *Cxcr7* (instead of its migratory-related counterpart *Cxcr4*). Then, a complete epithelialization occurs (leading to 'E' cells, *fully epithelial*), which amounts in a dramatic drop of their locomotion ability. Experimental studies further show that strong contact interactions between the overadhesive aPM individuals and dPM, pE and E agents are responsible for rosette stabilization.

The first PM → aPM transition and consequent rosette formation occur at the rostral edge of the primordium, while successive proto-neuromasts arise caudally to the last formed one. This results in a progressive confinement of PM individuals at the caudal edge of the primordium, which correlates with a restriction of the region of expression of Wnt (which triggers FGF10 secretion and avoids the expression of receptor *fgfr1*) [12]. It is, therefore, plausible that Wnt/Fgf signalling is related to the rise of point sources of FGF10 along the primordium and to the consequent proto-neuromast formation, but how PM individuals that will undergo activation are selected is still not completely understood. In this respect, in this work, we will not take into account Wnt/Fgf signalling pathways and consider a pre-patterned activation of PM individuals (see later). In more detail, we assume that
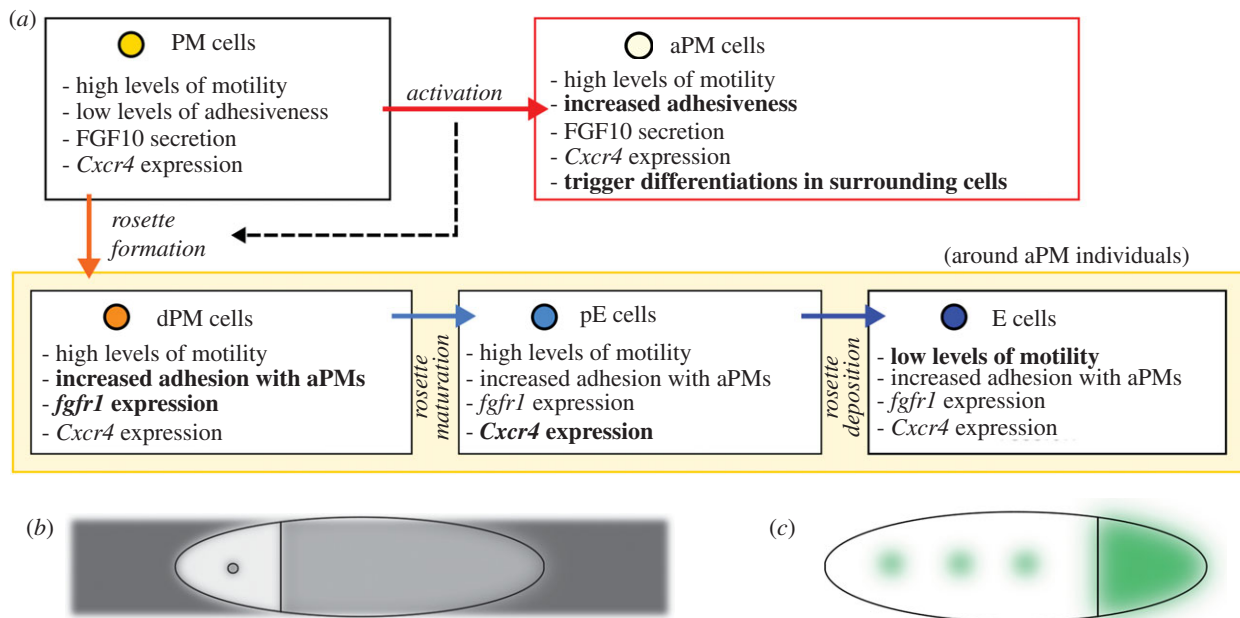
Figure 2. (*a*) Cell phenotypes and relative transitions regulating proto-neuromast formation, maturation and deposition. The black dashed arrow remarks that the three-step pseudo-mesenchymal-to-epithelial transitions (dPM → pE → E) in the central box occur only around an activated individual (i.e. they are triggered by the transition PM → aPM). (*b*) Typical regions of expression of the SDF1a receptors during primordium migration. The expression of the non-migratory receptor *Cxcr7* is always confined in the most rostral edge of the primordium (i.e. the rostral lighter area). The rest of the placode, as well as all aPM, express the migratory receptor *Cxcr4* (see the middle grey areas). *Cxcr7*-expressing cells sequester a higher amount of SDF1a (see the dark grey rectangle) than *Cxcr4*-expressing agents [11,13,16]. (*c*) Typical pattern of FGF10 during primordium migration. It is secreted by PM individuals at the caudal edge of the primordium and by aPM cells at the centre of proto-neuromasts (see the coloured regions), while all other individuals express the receptor *fgfr1* [5,11,16]. (Online version in colour.)

PM → aPM transitions are triggered by unknown stimuli, and that the formation and maturation of proto-neuromasts regulate the location of both FGF10 sources and the region of expression of *Cxcr4*/*Cxcr7* within the primordium, see figure 2*b,c*.

The embryonic development of the zebrafish PLL is mainly regulated by two diffusive chemicals. SDF1a, produced by the cells constituting the myoseptum substrate, forms around 20 hpf a homogeneous narrow stripe and represents an exogenous chemotactic cue for *Cxcr4* expressing individuals only (i.e. PMs, aPMs and dPMs). In this respect, the non-migratory-related receptor *Cxcr7* (expressed by pEs and Es) has an antagonistic effect against *Cxcr4*, owing to its enhanced affinity (estimated ten times higher). FGF10 is instead a placode endogenous substance which mainly plays as a short-range chemotactic cue for *fgfr1* expressing cells being indeed fundamental to preserve the primordium compactness over time.

(ii) Initial configuration and subsequent dynamics
Around 19 hpf, the progenitor PLL primordium is a homotypic placode of about 100 PM cells: it is characterized by an elliptical shape, elongated in the head-to-tail direction of the embryo, see again figure 1*a*. Soon a first rosette appears at the anterior/rostral edge of the cluster. Over the next hours, two or three additional proto-neuromasts sequentially form just caudally one to each other and the primordium begins to migrate along the homogeneous stripe of SDF1a, which is synthesized by the cells forming the horizontal myoseptum starting from about 20 hpf. The formation of a fourth caudal rosette then correlates with the deposition of the first formed (i.e. the most rostral) proto-neuromast, which slows down and detaches from the trailing edge of the primordium. Specifically, the movement of the overall primordium is allowed by the polarized expression of receptors *Cxcr4*/*Cxcr7* (see again figure 2*b*) which, owing to their different

affinity to their ligand, results in a self-generated local gradient of SDF1a underlying the placode. A cyclical behaviour is finally exhibited by the placode cluster: the assembly of a new rosette towards its caudal edge is in fact accompanied by the deposition of the most rostral one. This process is active until 46 hpf, i.e. when the primordium reaches the tip of embryo's tail and stops, and eventually results in the deposition of 6–8 proto-neuromasts, organized in a quite regular pattern along the trunk of the developing zebrafish, as sketched in figure 1*b*.

We finally remark that proliferation is fundamental to have a sufficient cell supply for rosette formation and deposition. Furthermore, regardless of the dynamics and phenotypic transitions, each component cell maintains an almost round morphology over time.

(b) Modelling background
The early development of zebrafish PLL has been recently approached also from a modelling perspective. Specifically, two-dimensional (2D) models have been provided in [11,20–23], a hybrid three-dimensional (3D) model is proposed in [16].

In [23], placode cells expressing receptor *Cxcr4* only have been reproduced with 2D lattice polygons, set to chemotactically move towards greater concentrations of SDF1a. These authors have also proposed a one-dimensional approximation of the system, which has allowed obtaining (i) a functional law relating the velocity of the primordium, its length and ligand/receptor dynamics and (ii) a connection between growth processes (when proliferation has been included), placode extension and deposition of discrete cell groups.

SDF1a-coordinated migration of the embryonic PLL has been analysed also in [11,21] by an agent-based model, built within the Netlogo programming environment. In particular, cells have been represented by mobile agents called

'turtles', reciprocally connected through visco-elastic links, which are able to express either *Cxcr4* or *Cxcr7*.

A model that takes into account both SDF1a and FGFs-related signalling pathways in regulating primordium locomotion was proposed in [20]. The cell aggregate has been represented as an elliptic continuum mass with embedded discrete motile individuals, that have been assumed to be viscoelastic and able to undergo large deformations. At the molecular level, both SDF1a-induced *Cxcr4/Cxcr7* signals and the FGFs-dependent Wnt/β-catenin pathways have been instead implemented by coupled reaction–diffusion (RD) equations.

In [22], the authors have then proposed a 2D hybrid approach which have also accounted for rosette formation. In particular, they have reproduced cells by discrete entities whose motion has been defined by second-order dynamics involving alignment, attraction and repulsion. They have also introduced the effects of FGFs and SDF1a signals (whose spatio-temporal evolutions have been described by proper RD equations) and of cell phenotypic transitions (regulated by proper rules), which are fundamental to reproduce the process of proto-neuromast assembly and maturation.

Finally, in [16], Knutsdottir and co-workers have developed a 3D model where the leading cells of the primordium have been hypothesized to produce FGFs, express Wnt receptors and sense gradients of SDF1a; while its trailing individuals have been conversely assumed to produce Wnt, express FGFs receptors, and sense gradients of FGFs. All individuals have been therein described as deformable ellipsoids of finite volume with mechanochemical interactions, i.e. adhesion, volume exclusion and chemokine-related active motion, whose phenotypes have been determined by the amount and the signalling network of Wnt/FGFs receptors. Cell proliferation has been included as well.

In this work, we conversely propose a multiscale hybrid model based on the assumptions reported in §2a, which thereby include (i) both SDF1a and FGF10 signaling regulating cell dynamics, (ii) both SDF1a-receptors *Cxcr4* and *Cxcr7*, (iii) the formation, maturation and deposition of proto-neuromasts, and (iv) cell proliferation, as specified in the next section.

3. Mathematical model

Our theoretical model, based on the previous list of assumptions, spans different scales: at the cellular level, the individuals composing the primordium are individually described as discrete interacting particles; at the subcellular level, the molecular substances (diffusive chemicals and receptors) are instead represented either with a continuous approach, i.e. through proper spatial distributions, or by Boolean binary variables. The overall mathematical framework indeed amounts to a hybrid system of first-order integro-differential equations for cell dynamics coupled with RD laws for chemical kinetics, and integrated by specific rules for phenotypic transitions and mitotic processes.

(a) System representation

The portion of the myoseptum involved in primordium development is schematically represented by a bidimensional bounded domain $\Omega \subset \mathbb{R}^2$, on the basis of the substantial thinness of the zebrafish embryo body. In particular, the left border of Ω represents the rostral edge of the myoseptum

(close to the embryo otic vesicle), whereas its right border indicates its caudal front (close to the tail of the embryo). Hereafter, $t \in [t_0, t_F]$ identifies the time (with t_0 and t_F as the initial and final values, respectively) and has units hpf.

Each cell forming the primordium is represented by a material point and labelled by an integer $i \in \{1, \dots, N(t)\}$, with the total number of individuals $N(t)$ that may vary in time owing to proliferation. The generic ith agent is characterized by the *state* variable $\tau_i(t) \in \{PM, aPM, dPM, pE, E\}$ and by a *sensing region*:

$$\mathcal{S}_i(t) = \{\mathbf{y} \in \Omega : |\mathbf{x}_i(t) - \mathbf{y}| \le d_a/2\}, \tag{3.1}$$

i.e. a bounded area where i is able to sense the presence of other individuals or of molecular substances, being d_a a sort of cell maximal extension, which also accounts for plasmamembrane protrusions. Cell body mean dimension is instead taken into account by a coefficient d_c.

The diffusive chemicals SDF1a and FGF10 are then described by spatial concentration variables, i.e. $\sigma(t, \mathbf{x})$, $\varphi(t, \mathbf{x}) : [t_0, t_F] \times \Omega \mapsto \mathbb{R}_+$, respectively.

Finally, the intracellular presence of the specific molecular receptors is quantified, for the sake of simplicity, by Boolean variables. In particular, $c_{\tau_i(t)}$ defines if agent i expresses SDF1a receptor *Cxcr4*, being

$$c_{\tau_i(t)}(t) = \{1, \text{ if } \tau_i(t) \in \{PM, aPM, dPM\}; \\ 0 \text{ if } \tau_i(t) \in \{pE, E\}. \tag{3.2}$$

It is useful to note that if $c_{\tau_i(t)} = 0$ for the generic ith particle, then it does not express the migration-related *Cxcr4* but rather the non migration-related *Cxcr7*. Coherently, $f_{\tau_i(t)}$ defines if agent i expresses FGF10 receptor *fgfr1* and reads as

$$f_{\tau_i(t)}(t) = \{1, \text{ if } \tau_i(t) \in \{dPM, pE, E\}; \\ 0, \text{ if } \tau_i(t) \in \{PM, aPM\}. \tag{3.3}$$

(b) Cell phenotypic transitions

The formation and stabilization of the proto-neuromasts are assumed to result from cyclical multi-step pseudo-mesenchymal-to-epithelial transitions (PM $\to$ dPM $\to$ pE $\to$ E) of localized rosettes of progenitor cells, triggered by the activation of a PM individual (PM $\to$ aPM), as sketched in figure 2a. In particular, the first activation of a progenitor PM is set to occur at a given $t_1 \approx 19$–20 hpf and involves the agent i_1 which is located almost along the main (horizontal) axis of the primordium at a characteristic distance $l^{PM \to aPM}$ from the rostral edge of the aggregate.

The following cyclical activations are delayed one from the other of a time lapse $\Delta t^{PM \to aPM}$ and involve the progenitor PM positioned along the horizontal axis of the placode with a relative distance equal to $2\,l^{PM \to aPM}$ from the previously activated individual. For instance, the generic i_kth PM cell undergoes such a phenotypic transition at $t_k = t_{k-1} + \Delta t^{PM \to aPM}$, being $k = 2, \dots, 8$, which amounts to a change in its state variable, i.e. $\tau_{i_k}(t_k) = aPM$.

Each activated PM i_k induces the gradual epithelialization of a surrounding cluster of progenitor PMs, that can be defined as

$$\mathcal{N}_{i_k}(t) = \{j \in \{1, \dots, N(t)\}, j \ne i_k : |\mathbf{x}_{i_k}(t) - \mathbf{x}_j(t)| \le d_a\}. \tag{3.4}$$

All agents falling within $\mathcal{N}_{i_k}$ are subjected to the following phenotypic changes: (i) at t_k, their state variable switches to dPM (i.e. $\tau_j(t_k) = dPM$); (ii) then after a characteristic time

equal to $\Delta t^{\mathrm{dPM}\to\mathrm{pE}}$, they assume a partial epithelial fate (i.e. $\tau_j(t_k + \Delta t^{\mathrm{dPM}\to\mathrm{pE}}) = \mathrm{pE}$); (iii) after another delay equal to $\Delta t^{\mathrm{pE}\to\mathrm{E}}$, they finally acquire a fully epithelial fate (i.e. $\tau_j(t_k + \Delta t^{\mathrm{dPM}\to\mathrm{pE}} + \Delta t^{\mathrm{pE}\to\mathrm{E}}) = \mathrm{E}$). The time lapse characteristic of each phenotypic transition is assumed to have a Gaussian distribution (with given mean and variance), which accounts both for experimental measures and of the randomness typical of biological systems.

(c) Cell proliferation

Cell proliferation is relevant mainly for progenitor PM cells. Without including all details relative to the mitotic cycle, we take into account a minimum period of time between successive duplications of the same individual and of a contact-inhibition of cell division in the case of high local cell density. In this respect, starting from $t_0 = 19$ hpf, every $\Delta t^{\mathrm{dupl}} = 1/\gamma_{\mathrm{dupl}}$, being γ_{dupl} a mitotic rate experimentally quantified in 2–4 mitosis h^{-1}, a PM cell is randomly selected and set to undergo duplication if it is sufficiently far from the other agents (i.e. if $d_{i,\min}(t) := \min_{j=1,\dots,N(t),j\neq i} |\mathbf{x}_i(t) - \mathbf{x}_j(t)| > d_{\mathrm{dupl}}$, being $d_{\mathrm{dupl}} < d_{\mathrm{c}}$ a sort of cell perinuclear region). A newborn agent, labelled by the identity integer $N(t)+1$, is then added to the system close to the parent position, i.e. $\mathbf{x}_{N(t)+1}(t) = \mathbf{x}_i(t) + (d_{\mathrm{c}}/2)\,(\cos(\eta_i(t));\,\sin(\eta_i(t)))$, being $\eta_i(t)$ a random angle uniformly distributed over $[0, 2\pi)$. The daughter cell then inherits from the progenitor the phenotype (i.e. $\tau_{N(t)+1}(t) = \tau_i(t) = \mathrm{PM}$), while its dynamics will be completely autonomous.

(d) Cell dynamics

Cell spatial distribution evolves in time according to a set of first-order integro-differential equations, which can be formally derived from a second-order Newtonian approach under the assumption of an overdamped-velocity response (see [24–26] and references therein for further comments):

$$\frac{\mathrm{d}\mathbf{x}_i}{\mathrm{d}t}(t) = \mu_{\tau_i(t)}(t)\mathbf{v}_i(t), \quad i = 1, \dots, N(t). \tag{3.5}$$

In equation (3.5), $\mu_{\tau_i(t)}$ is a dimensionless motility coefficient that depends on the phenotype of the individual of interest and also takes into account cell-substrate friction mechanisms. In particular, $\mu_{\tau_i(t)} = 1$ if $\tau_i(t) \in \{\mathrm{PM, aPM, dPM, pE}\}$ and $\mu_{\tau_i(t)} = 0.1$ if $\tau_i(t) = \mathrm{E}$ because, as already explained, fully epithelial individuals have a drop in their migratory ability. The velocity $\mathbf{v}_i$ of the generic agent i is then assumed to result from the superposition of different contributions:

$$\mathbf{v}_i(t) = \mathbf{v}_i^{\mathrm{int}}(t) + \mathbf{v}_i^{\mathrm{fgf}}(t) + \mathbf{v}_i^{\mathrm{sdf}}(t) + \mathbf{v}_i^{\mathrm{rand}}(t),$$
$$i = 1, \dots, N(t), \tag{3.6}$$

where $\mathbf{v}_i^{\mathrm{int}}$ is the contribution relative to intercellular direct contacts, $\mathbf{v}_i^{\mathrm{fgf}}$ and $\mathbf{v}_i^{\mathrm{sdf}}$ implement directional chemotactic movements owing to the presence of FGF10 and SDF1a, respectively, as mediated by the specific receptors (when expressed), and $\mathbf{v}_i^{\mathrm{rand}}$ finally describes the random crawling movement typical of biological individuals.

Entering in more details, cell-cell direct interactions classically include either short-range repulsive or middle-range adhesive dynamics. Specifically, two cells tend to repel each other when they fall too close. On the other hand, cell-cell adhesion arises from the activity of cadherins which implies that two cells can form contact junctions only when their

relative distance is lower than the maximal extension of their membrane protrusions. Furthermore, both repulsive and adhesive velocity components result from the superimposition of binary (pairwise) contributions, each aligned to the line ideally connecting the two interacting individuals:

$$\mathbf{v}_i^{\mathrm{int}}(t) = \sum_{\substack{j=1\\j\neq i}}^{N(t)} \mathbf{v}_{ij}^{\mathrm{int}}(t) = \sum_{\substack{j=1\\j\neq i}}^{N(t)} (\mathbf{v}_{ij}^{\mathrm{rep}}(t) + \mathbf{v}_{ij}^{\mathrm{adh}}(t))$$

$$= \sum_{\substack{j=1\\j\neq i}}^{N(t)} (K_{\mathrm{rep}}(|\mathbf{r}_{ij}(t)|) + K_{\mathrm{adh}}^{\tau_i(t)\tau_j(t)}(|\mathbf{r}_{ij}(t)|)) \frac{\mathbf{r}_{ij}(t)}{|\mathbf{r}_{ij}(t)|}, \tag{3.7}$$

being $\mathbf{r}_{ij}(t) := \mathbf{x}_j(t) - \mathbf{x}_i$. Kernels $K_{\mathrm{rep}} : \mathbb{R}_+ \cup \{0\} \mapsto \mathbb{R}_- \cup \{0\}$ and $K_{\mathrm{adh}}^{\tau_i(t)\tau_j(t)} : \mathbb{R}_+ \cup \{0\} \mapsto \mathbb{R}_+ \cup \{0\}$ model the strength of the repulsive and adhesive pairwise stimuli, respectively, the former being independent from the specific pair of individuals involved and the latter strongly correlated to the phenotype of the interacting agents (as experimentally demonstrated and previously commented). In particular, we opt for a hyperbolic-like repulsive behaviour, i.e.:

$$K_{\mathrm{rep}}(z) = \left\{ v_{\mathrm{rep}}\left(1 - \frac{d_{\mathrm{c}}}{z}\right), \text{ if } z \in (0, d_{\mathrm{c}}); \ 0, \text{ otherwise} \right\},$$
$$\tag{3.8}$$

and parabolic-like attractive dynamics, i.e.:

$$K_{\mathrm{adh}}^{\tau_i(t)\tau_j(t)}(z) = \left\{ v_{\mathrm{adh}}^{\tau_i(t)\tau_j(t)}\left(1 - \frac{z^2}{d_{\mathrm{a}}^2}\right), \text{ if } z \in (0, d_{\mathrm{a}}); \ 0, \text{ otherwise} \right\}.$$
$$\tag{3.9}$$

In equations (3.8) and (3.9), the positive coefficients v_{rep} and $v_{\mathrm{adh}}^{\tau_i(t)\tau_j(t)}$, which have speed units, are related to cell stiffness and to the level (and the activity) of cell membrane adhesive proteins, respectively. In accordance with the biological considerations, we indeed set

$$v_{\mathrm{adh}}^{\tau_i(t)\tau_j(t)} = \{V_{\mathrm{adh}}, \text{ if } \tau_i(t) = \mathrm{aPM} \text{ and }$$
$$\tau_j(t) \in \{\mathrm{dPM, pE, E}\} \text{ or vice versa;}$$
$$v_{\mathrm{adh}}, \text{ otherwise}\}, \tag{3.10}$$

being with $V_{\mathrm{adh}} > v_{\mathrm{adh}}$, see figure 3.

Cells expressing the receptor *fgfr1*, i.e. dPM, pE and E individuals (with $f_{\tau_i(t)}(t) = 1$), experience an attractive force towards higher amounts of FGF10 they detect within their actual sensing region $\mathcal{S}_i(t)$. The velocity component $\mathbf{v}_i^{\mathrm{fgf}}$ implements the FGF10 dose-dependent chemotactic motion of *fgfr1*-expressing individuals (i.e. dPM, pE and E cells):

$$\mathbf{v}_i^{\mathrm{fgf}}(t) = \frac{f_{\tau_i(t)}(t)\chi_{\mathrm{fgf}}}{\varphi_{\max}A(\mathcal{S}_i(t))} \int_{\mathcal{S}_i(t)} W_i^{\mathrm{fgf}}(t, \mathbf{y})\,\varphi(t, \mathbf{y})\,(\mathbf{y} - \mathbf{x}_i(t))\,\mathrm{d}\mathbf{y}, \tag{3.11}$$

where $f_{\tau_i(t)}$ is the Boolean variable introduced in equation (3.3), χ_{fgf} denotes a cell chemical sensitivity to FGF10, and the quantity $\varphi_{\max}A(\mathcal{S}_i(t))$ measures the maximal amount of FGF10 that agent i can perceive within its sensing region, being $A(\mathcal{S}_i(t))$ the actual extension of $\mathcal{S}_i(t)$ and $\varphi_{\max}$ the maximal concentration experimentally found. Finally, the weight function

$$W_i^{\mathrm{fgf}}(t, \mathbf{y}) = \left(1 + \sum_{\substack{j=1, j\neq i\\ \tau_j(t)\in\{\mathrm{dPM, pE, E}\}}}^{N(t)} \mathbf{1}_{\mathcal{S}_j(t)}(\mathbf{y}) \right)^{-1}, \tag{3.12}$$
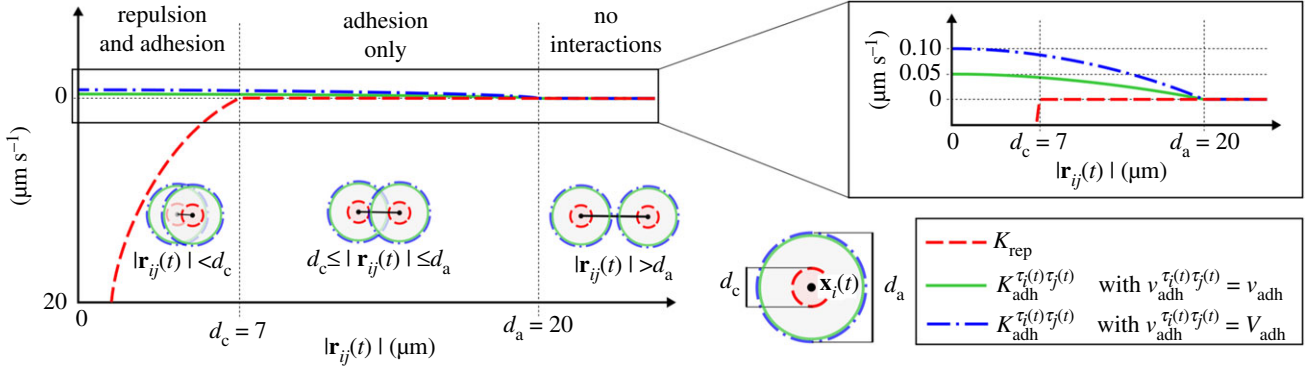
Figure 3. Plot of the kernels K_{rep} and $K_{\text{adh}}^{\tau_i(t)\tau_j(t)}$ given in equations (3.8) and (3.9), as used in the numerical simulations. Red dashed line: K_{rep} with $d_c = 7\,\mu\text{m}$ and $v_{\text{rep}} = 10\,\mu\text{m s}^{-1}$. Green solid line: $K_{\text{adh}}^{\tau_i(t)\tau_j(t)}$ with $d_a = 20\,\mu\text{m}$ and $v_{\text{adh}} = 0.05\,\mu\text{m s}^{-1}$. Blue dash-dot line: $K_{\text{adh}}^{\tau_i(t)\tau_j(t)}$ with $d_a = 20\,\mu\text{m}$ and $V_{\text{adh}} = 0.1\,\mu\text{m s}^{-1}$. (Online version in colour.)

being $\mathbf{1}_{(\cdot)}$ the indicator function, accounts for the competing effect of other *fgfr1*-expressing cells possibly extending over $\mathcal{S}_i(t)$, each of them sequestering a portion of the local amount of FGF10 molecules.

On the other hand, PM, aPM and dPM cells expressing *Cxcr4* (with $c_{\tau_i(t)}(t) = 1$) are attracted towards higher amounts of SDF1a they detect within their sensing region $\mathcal{S}_i(t)$. An expression analogous to that in equation (3.11) is therefore set for SDF1a-induced directional contribution:

$$\mathbf{v}_i^{\text{sdf}}(t) = \frac{c_{\tau_i(t)}(t)\chi_{\text{sdf}}}{\sigma_{\max}A(\mathcal{S}_i(t))}\int_{\mathcal{S}_i(t)} W_i^{\text{sdf}}(t,\mathbf{y})\,\sigma(t,\mathbf{y})\,(\mathbf{y}-\mathbf{x}_i(t))\,\mathrm{d}\mathbf{y},$$

$$(3.13)$$

being $c_{\tau_i(t)}$ the binary variable introduced in equation (3.2) identifying the presence of migration-related ligand *Cxcr4*, and χ_{sdf} a cell chemical sensitivity to SDF1a, and $\sigma_{\max}A(\mathcal{S}_i(t))$ measures the maximal amount of SDF1a that cell i can perceive within its sensing region. The weight function W_i^{sdf} has the same role as its counterpart introduced in equation (3.11), but here it has to take into account the fact that (i) both SDF1a receptors sequester a portion of their ligand, and that (ii) the non-migratory-related receptor *Cxcr7* has a much higher affinity with SDF1a than the migratory-related *Cxcr4*. In this respect, we set

$$W_i^{\text{sdf}}(t,\mathbf{y})$$

$$= \left(1 + \sum_{\substack{j=1,j\neq i \\ \tau_i(t)\in\{\text{PM,aPM,dPM}\}}}^{N(t)} \alpha_4^{\text{sdf}}\mathbf{1}_{\mathcal{S}_j(t)}(\mathbf{y}) + \sum_{\substack{j=1,j\neq i \\ \tau_i(t)\in\{\text{pE,E}\}}}^{N(t)} \alpha_7^{\text{sdf}}\mathbf{1}_{\mathcal{S}_j(t)}(\mathbf{y})\right)^{-1},$$

$$(3.14)$$

with α_4^{sdf}, $\alpha_7^{\text{sdf}} \in (0,1]$ and $\alpha_4^{\text{sdf}} \ll \alpha_7^{\text{sdf}}$, where α_4^{sdf} and α_7^{sdf} denote the affinity for SDF1a of receptor *Cxcr4* and *Cxcr7*, respectively.

Brownian fluctuations typical of biological individuals are finally implemented, for each generic agent i, by $\mathbf{v}_i^{\text{rand}}(t) = v_{\text{rand}}(\cos(\theta_i(t)),\sin(\theta_i(t)))$, where $\theta_i(t)$ is a random angle uniformly distributed over $[0,2\pi)$ and v_{rand} is a mean primordium speed.

(e) Chemical kinetics

FGF10 is produced within the entire sensing region of PM and aPM individuals (until a limit). It then homogenously diffuses in the surrounding environment and degrade at a constant rate as described by the following RD equation

$$\frac{\partial \varphi}{\partial t}(\mathbf{x},t) = D_\varphi\Delta\varphi(\mathbf{x},t)$$

$$+ \left(1 - \frac{\varphi(\mathbf{x},t)}{\varphi_{\max}}\right)\times \sum_{\substack{i=1 \\ \tau_i(t)\in\{\text{PM,PM}\}}}^{N(t)} \gamma_\varphi\mathbf{1}_{\mathcal{S}_i(t)}(\mathbf{x},t) - \delta_\varphi\varphi(\mathbf{x},t),$$

$$(3.15)$$

where D_φ is the diffusion coefficient, while γ_φ and δ_φ are the constant production and the decay rate, respectively.

SDF1a is secreted at a constant rate over a narrow stripe $\mathcal{H}\subset\Omega$ of the horizontal myoseptum, starting from $t_{\text{sdf}} = 20\,\text{hpf}$. It then poorly diffuses and decays within the surrounding environment, quickly stabilizing in a quasi-homogeneous pattern, as

$$\frac{\partial \sigma}{\partial t}(\mathbf{x},t) = D_\sigma\Delta\sigma(\mathbf{x},t)$$

$$+ \left(1 - \frac{\sigma(\mathbf{x},t)}{\sigma_{\max}}\right)\gamma_\sigma\mathbf{1}_{\mathcal{H}}(\mathbf{x},t)H(t-t_{\text{sdf}}) - \delta_\sigma\sigma(\mathbf{x},t),$$

$$(3.16)$$

being D_σ the diffusion coefficient, γ_σ and δ_σ the constant production and decay rate, respectively, and H the Heaviside function.

4. Numerical results

In this section, we will first give simulation details and comments on the parameter estimate. We will then present and analyse numerical realizations able to describe both the physiological (i.e. normal) development of the zebrafish PLL and selected experimental manipulations involving placode laser dissection. In both cases, a qualitative analysis of system behaviour upon variations in the values of the free model parameters, i.e. repulsive/adhesive interactions, cell chemical sensitivity and SDF1a internalization rates, is provided. The aim of these studies is both to further analyse the proposed model by validating the model and the estimated values reported in table 1, but also to provide some predictive insights in the absence of experimental counterparts.

Table 1. List of model parameters. ($\mathcal{N}(\mu, s)$ denotes a Gaussian distribution characterized by mean μ and variance s.)

parameter	description	value	reference
Ω	spatial domain	$[0, 2000] \times [0, 100]\ \mu m^2$	[3,15,27]
$\mathcal{H}$	region where SDF1a is produced	$[0, 2000]\ \mu m \times [40, 60]\ \mu m$	[3,15,27]
$[t_0, t_F]$	period of observation	$[19, 46]$ hpf	[15]
d_a	maximal extension of cell membrane protrusions	$20\ \mu m$	[22,24]
d_c	mean diameter of cell body	$7\ \mu m$	[15]
d_{dupl}	mean diameter of cell perinuclear region	$6\ \mu m$	[15]
γ_{dupl}	PM cell proliferation rate	4 mitoses h^{-1}	[15]
$l^{PM \rightarrow aPM}$	distance of first aPM from primordium rostral edge	$16.5\ \mu m$	[5]
t_1	instant time of first activation of a PM	19.5 hpf	[5]
$\Delta t^{PM \rightarrow aPM}$	time lapse between successive activations of PMs	$\mathcal{N}(3.07\ h, 1.44\ h)$	[5,17,28]
$\Delta t^{dPM \rightarrow pE}$	time lapse between PM deactivation and its partial epithelialization	$\mathcal{N}(4.2\ h, 1.12\ h)$	[5,17,28]
$\Delta t^{pE \rightarrow E}$	time lapse between partial and full epithelialization of a cell	$\mathcal{N}(4\ h, 1.17\ h)$	[5,17,28]
D_φ	diffusion coefficient of FGF10	$10\ \mu m^2\ s^{-1}$	[16]
φ_{max}	maximal concentration of FGF10	1.5 nM	[16]
γ_φ	FGF10 secretion rate	0.0083 nM s^{-1}	[16]
δ_φ	FGF10 decay rate	$0.0025\ s^{-1}$	[16]
D_σ	diffusion coefficient of SDF1a	$0.333\ \mu m^2\ s^{-1}$	[16]
σ_{max}	maximal concentration of SDF1a	0.5 nM	[16]
γ_σ	SDF1a secretion rate	0.0033 nM s^{-1}	[16]
t_{sdf}	instant time of SDF1a onset	20 hpf	[16]
δ_σ	SDF1a decay rate	$0.0033\ s^{-1}$	[16]
v_{rand}	mean speed of the primordium	$0.019\ \mu m\ s^{-1}$	[5]
v_{rep}	strength of repulsive interactions	$10\ \mu m\ s^{-1}$	data fitting
v_{adh}	strength of adhesive interactions	$0.05\ \mu m\ s^{-1}$	data fitting
V_{adh}	strength of overadhesive interactions	$0.1\ \mu m\ s^{-1}$	data fitting
χ_{fgf}	level of activity of FGF10 receptor *fgfr1*	$0.02\ \mu m^2\ s^{-1}$	data fitting
χ_{sdf}	level of activity of SDF1a receptor *Cxcr4*	$0.2\ \mu m^2\ s^{-1}$	data fitting
α_4^{sdf}	affinity between SDF1a and its receptor *Cxcr4*	0.05	data fitting
α_7^{sdf}	affinity between SDF1a and its receptor *Cxcr7*	0.5	data fitting

(a) Numerical approximation and computational details

The method used in the numerical simulations employs a finite volume method with implicit Euler scheme in time and a central difference scheme in space for the solution of equations (3.15) and (3.16). Equation (3.6) is conversely solved by applying the explicit Euler scheme in time.

In this respect, the spatial domain Ω is divided into squared control volumes $Q_{m,n}$ of side $\Delta x = 2\ \mu m$, which are identified by their centres $\mathbf{x}_{m,n} := (x_m, y_n)$, being $x_m = (m - 1/2)\Delta x$ and $y_n = (n - 1/2)\Delta x$, with $m = 1, \ldots, 1000$ and $n = 1, \ldots, 50$. The time interval $[t_0, t_F]$ is conversely divided into subintervals of length $\Delta t = 0.25\ s$ (so that $\Delta x / \max_i\{\mathbf{v}_i\} < \Delta t$ for any t), and the kth time step is denoted by $t_k := k\Delta t$ with $k \in \mathbb{N}$.

At any time step t_k, the spatial distributions $\sigma(t_k, \mathbf{x})$ and $\varphi(t_k, \mathbf{x})$ are, respectively, approximated by piecewise-constant distributions $\sigma^k, \varphi^k : \Omega \mapsto \mathbb{R}_+$ such that $\sigma^k(\mathbf{x})\ |_{Q_{m,n}} = \sigma(t_k, \mathbf{x}_{m,n})$ and $\varphi^k(\mathbf{x})\ |_{Q_{m,n}} = \varphi(t_k, \mathbf{x}_{m,n})$, for any $m = 1, \ldots, 1000$ and $n = 1, \ldots, 50$. Analogously, the indicator function $\mathbf{1}_{(\cdot)}(\mathbf{x})$, in equations (3.12) and (3.14)–(3.16), is approximated by a piecewise-constant function too, i.e. $\widehat{\mathbf{1}}_{(\cdot)} : \Omega \mapsto \mathbb{R}_+$ such that $\widehat{\mathbf{1}}_{(\cdot)}(\mathbf{x})\ |_{Q_{m,n}} = 1$ if $\mathbf{x}_{m,n} \in (\cdot)$, and $\widehat{\mathbf{1}}_{(\cdot)}(\mathbf{x})\ |_{Q_{m,n}} = 0$ otherwise. At

any time step t_k, the functions $W_i^{fgf}(t_k, \mathbf{x})$ and $W_i^{sdf}(t_k, \mathbf{x})$ in equations (3.12) and (3.14) are, therefore, approximated by $W_i^{fgf,k}$ and $W_i^{sdf,k}$, respectively, obtained by substituting the indicator function with $\widehat{\mathbf{1}}_{S_j(t_k)}$. The integrands in equations (3.11) and (3.13) are therefore computed by a 2D quadrature formula, which consists of a sum of the discretized integrand function on the control volumes $Q_{m,n}$ whose centre $\mathbf{x}_{m,n}$ actually belongs to the neighbourhood $S_i(t_k)$.

The time-stepping then proceeds as follows: (i) the system is initiated and the time lapses characterizing cell phenotypic transitions are randomly selected; (ii) the local available fraction of chemicals $W_i^{fgf,k}$ and $W_i^{sdf,k}$ are computed for any i (see equations (3.12) and (3.14)); (iii) cell velocity components in equation (3.6) are calculated for any i; (iv) cells are moved according to equation (3.5); (v) cell phenotypic transitions may occur; (vi) cell duplication may occur; (vii) the distributions of FGF10 and SDF1a are updated according to equations (3.15) and (3.16); and (viii) points (ii)–(vii) are repeated for any time step.

The method is implemented by a software written in C++ which can not be disclosed being partially property of the

Optimad Engineering s.r.l. The 2D output images are generated with the free software GNUPLOT.

(b) Simulation details and parameter estimate

The period of observation of each simulation is consistently included in the time lapse [$t_0 = 19$, $t_F = 46$] hpf, which characterizes the entire phenomenon of primordium migration and rosette formation and maturation. The computational domain Ω is a rectangular $2000 \times 100 \, \mu m^2$ area, that represents the horizontal myoseptum. As a remark, the left and right border of Ω computationally define the rostral and the caudal edge of the myoseptum, respectively, the former being close to the optic vesicle and the latter to the tail of the animal. The region $\mathcal{H}$, reproducing the stripe where the SDF1a is produced by the substrate, extends over the region [0, 2000] $\mu m \times$ [40, 60] μm, in accordance with [3,15,27]. The domain boundary $\partial\Omega$ is then assumed to be a physical barrier because it implements the wall of somites that encloses the myoseptum. Because they have the capacity to internalize FGF10 but not SDF1a, we provide equation (3.15) with a homogeneous Dirichlet condition and equation (3.16) with a no-flux condition. Finally, equation (3.5) is equipped by proper rules that force cells to bounce back when they touch or try to move across the boundary of Ω. Initially, there are no chemicals in the system.

The proposed approach is intrinsically multiparametric, being characterized by a number of model coefficients, all listed in table 1. Most of them have a clear empirical counterpart, and therefore we have directly inherited their values from the experimental literature, specifically (i) cell dimensions, (ii) proliferation rates, (iii) means and variances of the characteristic times of individual phenotypic transitions, (iv) coefficients regulating chemical kinetics, and (v) mean primordium speed. In particular, the values of the coefficients regulating chemical kinetics are chosen on the basis of the estimates proposed by Knuttsdottir *et al.* in [16]; while the others are set according to direct measurements reported in the literature. The remaining set of model coefficients is somehow more technical. In this respect, for the sake of simplicity, we have further assumed that (i) $V_{adh} = 2v_{adh}$, consistently with [16]; (ii) $v_{adh}^{\tau_i(t)\tau_j(t)}/v_{rep} < 5d_c^3/4d_a^3$ (in particular, we have fixed $v_{adh}/v_{rep} = 0.005$ and $V_{adh}/v_{rep} = 0.01$) so that the interactions laws result H-stable, see recent works in [24,29,30] and references therein; and (iii) $\alpha_7^{sdf} = 10\alpha_4^{sdf}$ with $\alpha_4^{sdf} \in (0, 0.1]$ and $\alpha_7^{sdf} \in (0, 1]$, according to [13]. For the estimate of the remaining parameters, i.e. v_{rep} (or v_{adh} and V_{adh}), χ_{fgf}, χ_{sdf} and α_4^{sdf}, we have run preliminary simulations of the normal PLL development and fitted the resulting outcomes with the corresponding empirical evidence, both qualitatively and quantitatively (i.e. in terms of morphology and effective mean placode velocity). Specifically, we look for the set of parameter values that results in both (i) an elongation of the placode before the beginning of its migration (said L) within the range [140, 175] μm, according to [15]; and (ii) an effective mean primordium speed (said v_{PLL}) in the range [0.018, 0.02] $\mu m \, s^{-1}$, accounting for measurements in [5]. With this strategy, we have fixed reasonable values for adhesion/repulsion coefficients (i.e. v_{rep}, v_{adh} and V_{adh}), cell chemical sensitivity (i.e. χ_{sdf} and χ_{fgf}) and SDF1a internalization rates (i.e. α_4^{sdf} and α_7^{sdf}).

All the forthcoming numerical simulations have been performed 10 times. The absence of large variations in system behaviour allowed us to report a representative realization of each series of simulations.

(c) Reference simulation

The aim of this reference simulation is to reproduce the physiological development of the zebrafish PLL, i.e. that occurring in so-called *wild-type* embryo. At the initial time instant $t_0 = 19$ hpf, see figure 4a, the primordium is an ellipsoidal cluster constituted by $N(t_0) = 100$ pseudo-mesenchymal progenitor cells (i.e. with the common type PM), located at the rostral (left) edge of the domain Ω. At $t_1 = 19.5$ hpf, see figure 4b, a PM individual in the rostral part of the primordium differentiates and induces the deactivation of the cells in its surroundings. After a while, i.e. at $t_{sdf} = 20$ hpf, see figure 4c, the exogenous SDF1a starts to be produced by the substrate, thereby initiating the mechanisms underlying the directional migration of the aggregate. In particular, the placode first remains fixed, while elongating along the stripe of the chemical, see figure 4d. Both the PM agents at the leading edge of the proto-organ and the dPM individuals forming the rosette body at its trailing edge in fact express the migratory receptor *Cxcr4* and extend towards the SDF1a: this results in a force balance that inhibits the overall movement of the cluster, as also observed in [13]. At $t_2 = 22$ hpf, see figure 4e, a second rosette-like cluster assembles, just caudally to the first proto-neuromast. Soon after, see figure 4f, the primordium begins to actively migrate: dPM cells forming the first rosette in fact undergo partial epithelialization, thereby not longer expressing *Cxcr4* but its not-migratory-related counterpart *Cxcr7*. As a consequence, only the caudal part of the primordium is subjected to the SDF1a-induced velocity contribution being therefore free to advance, eventually dragging the entire embryonic organ though adhesive interactions and FGF10-related dynamics.

During migration, additional rosettes sequentially form towards the caudal region of the aggregate, see figure 4g,h. Just after the assembly of the fourth proto-neuromast, pE particles forming the most rostral rosette (i.e. the firstly formed) undergo full epithelialization (because the time-lapse needed for the corresponding phenotypic transitions has occurred), see figure 4i. This results in a drop of their migratory ability and causes the arrest of the entire cluster which separates from the rest of the placode, being deposited within the myoseptum, as a consequence also of its intrinsic compactness owing to the enhanced adhesiveness of the central aPM agent.

Subsequently a cyclical behaviour occurs. It amounts in a succession of rosette deposition from the rostral edge of the primordium and proto-neuromast assembly at its caudal area, see figure 4j,k. At the end of the observation period, i.e. at $t_F = 46$ hpf, see figure 4l, the embryonic PLL comprises five deposited proto-neuromasts and three terminal rosettes which form the remaining main body of the primordium. Interestingly, the proposed reference simulation (which is characterized by $L \approx 166 \, \mu m$ and $v_{PLL} \approx 0.02 \, \mu m \, s^{-1}$) is in good agreement with biological evidence also in terms of distance between pairs of deposited proto-neuromasts which ranges between (240, 280) μm, close to the experimental counterparts [3,15].

In order to further justify the employed estimate for the model parameters, a qualitative analysis of the dependence of the critical quantities L and v_{PLL} from the adhesion/repulsion coefficients, cell chemical sensitivity and SDF1a internalization
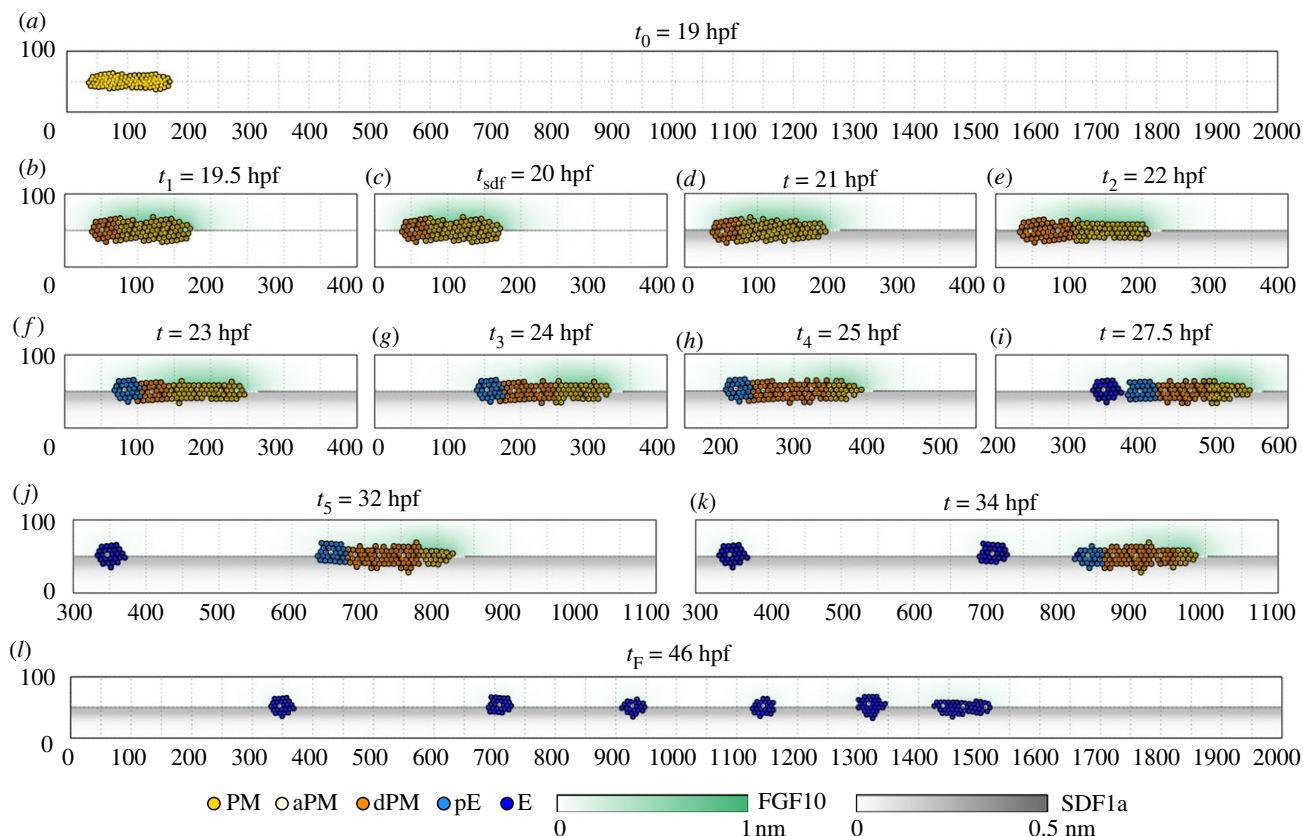
Figure 4. Representative frames of the reference simulation. Cells are represented by circles with diameter d_c. As a remark, FGF10 is secreted by PM and aPM cells; while dPM, pE and E agents express the FGF receptor fgfr1. The migratory-related SDF1a receptor Cxcr4 is expressed by PM aPM and dPM inviduals, while pE and E cells express the not-migratory related Cxcr7. Refer to figure 2a for a summary of cell phenotypic characterization. For visualization purposes, hereafter, we plot $\varphi(t, \mathbf{x})$ in the upper half of the domain (green shadow), and $\sigma(t, \mathbf{x})$ in the lower half of Ω (grey shadow), by taking advantage of the substantial horizontal symmetry of both FGF10 and SDF1a distributions. (Online version in colour.)
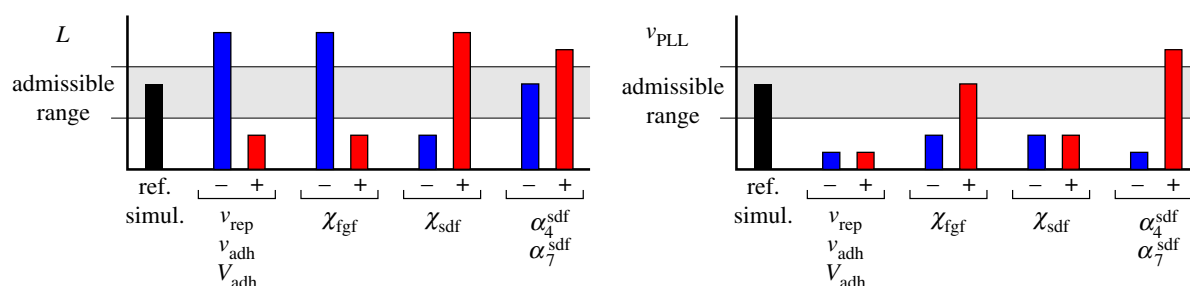

Figure 5. Variation of the critical quantities L and v_{PLL} upon variations in the free model parameters: i.e. the adhesion/repulsion coefficients (i.e. v_{rep}, v_{adh} and V_{adh}), cell chemical sensitivity (i.e. χ_{fgf} or χ_{sdf}) and SDF1a internalization rates (i.e. α_4^{sdf} and α_7^{sdf}). In both plots, the grey regions denote the range of admissible values, i.e. [140, 175] μm for L and [0.018, 0.02] μm s^{-1} for v_{PLL}. Black (most left) columns refer to the reference simulation in figure 4. Model outcomes obtained by decreasing or increasing a parameter are represented by blue (left) and red (right) columns respectively. (Online version in colour.)

rates are provided in figure 5. In particular, we deal with model outcomes in the case of decrease/increase of the value of one of the referred parameters.

In detail, figure 5a shows that the primordium results excessively elongated before migration in the case of either too low interaction coefficients (i.e. v_{rep}, v_{adh} and V_{adh}), too low cell chemical sensitivity to FGF10 (i.e. χ_{sdf}), or too high SDF1a-related parameters (i.e. χ_{sdf} or α_4^{sdf} and α_7^{sdf}). Conversely, too high interaction coefficients, too high cell chemical sensitivity to FGF10, or too low SDF1a-related parameters result in a more compact and rounder configuration. More in detail, a decrease/increase in the interaction coefficients (having fixed the ratios v_{adh}/v_{rep} and V_{adh}/v_{rep}) mainly corresponds to a drop/raise in cell-cell adhesive dynamics by preserving admissible minimal intercellular distances (see [24]). It thereby

increases/reduces cell ability to detach from the rest of the aggregates and explains the observed stretched/compressed configurations. Similarly, variations in χ_{fgf} affect the attraction experienced by fgfr1-expressing cells (i.e. dPM, focusing of primordium elongation before migration) towards cells secreting FGF10 at the centre of the rosettes (aPMs) and at the caudal edge of the placode (PMs). Decreases/increases in χ_{fgf} thus contribute to the reduction/increment of the cohesion of cells within the PLL proto-organ. Therefore, both interaction coefficients and FGF10-related parameter regulate primordium cohesion. On the other hand, an increase/decrease in cell sensitivity to SDF1a, i.e. χ_{sdf}, translates in a stronger/deeper attraction of Cxcr4 expressing cells toward higher amounts of SDF1a: cells at the caudal/rostral edges are more/less attracted towards embryo's tail/head, while cells at the top/

10

royalsocietypublishing.org/journal/rstb   Phil. Trans. R. Soc. B 375: 20190385

bottom edges of the placode are attracted towards the central horizontal axis of the domain. Finally, in the case of too high affinity of both $Cxcr4/Cxcr7$ to SDF1a, i.e. of both α_4^{sdf} and α_7^{sdf}, cells almost completely sequester the chemical located in their sensory regions, thereby leading to a steeper self-generated gradient underlying the primordium which increases primordium elongation.

Referring again to figure 5, we can further note that a decrease in both α_4^{sdf} and α_7^{sdf}, does not affect the placode elongation before migration (left panel), however, it results in an excessive slowdown of primordium migration (right panel). An extremely low affinity of SDF1a receptors to their ligand in fact implements an almost negligible internalization of the local chemical by cells, quantified by $W_i^{sdf} \approx 1$. It therefore prevents the emergence of the self-generated local gradient of SDF1a underlying primordium locomotion despite the polarized expression of $Cxcr4/Cxcr7$ along the placode. Conversely, in all the other cases, anomalies in the initial elongation of the primordium result in an abnormal locomotion of the placode.

Consistently with the numerical results reported in figure 5, experimental outcomes have shown that drops in primordium directional speed occur upon either the disruption of the activity of cell surface receptor $fgfr1$ [5,17], or upon the inhibition of the expression/activity of SDF1a migratory-related receptor $Cxcr4$ [1,28]. Moreover, the absence of SDF1a signalling has been shown to result in a more round and compact morphology [1,28]. In this perspective, our study first validates the proposed model and the estimated parameter values reported in table 1, but also gives predictive insights on manipulations that have not yet an experimental counterpart (i.e. variations in cell-cell interactions and in SDF1a internalization rates).

(d) Laser dissections

We then mimic a series of experiments of laser ablation performed in [11]. A first type of manipulation in this respect, based also on an *assay* proposed in [31], amounts to dividing the primordium into two fragments: a small leading/caudal cluster formed by 10–20 $Cxcr4$-expressing cells *only*, and a trailing/rostral aggregate which instead contains *also* individuals expressing $Cxcr7$. *In silico*, see figure 6, the configuration of the placode corresponding to the proposed *in vitro* setting consists of allowing the normal development of the primordium until 28 hpf, i.e. until the deposition of the first rosette and the maturation of the second one, and then in removing a group of cells. Before ablation, the PLL proto-organ is constituted (going from left to right) by a deposited rosette (with E cells) and a migrating placode comprising a rostral mature proto-neuromast with pE agents, two rosettes with dPM cells, and a leading group of PM individuals (as in figure 4i). The configuration in figure 6a is then obtained by removing a cluster of progenitor PM cells just behind the head of the main mass of the migrating primordium, and by neglecting the presence of the deposited proto-neuromast. Consistently with the phenotypic characterization employed so far, the remaining caudal fragment is in fact formed by $Cxcr4$-expressing PM individuals only, whereas the trailing portion is formed by $Cxcr7$-expressing pE agents, as well as by aPM (the centre of the rosettes) and dPM cells, all having $Cxcr4$. The initial gap between the two clusters is larger than $2d_a$, i.e. laser ablation initially inhibits adhesive
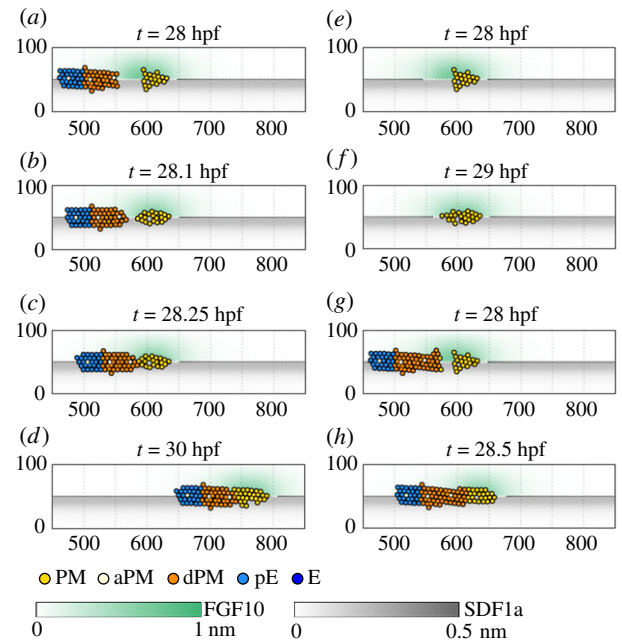

Figure 6. Numerical simulations reproducing experiments performed in [11,31] where the migrating primordium is divided into two fragments via laser ablation: a small leading/caudal cluster comprising individuals expressing $Cxcr4$ only (i.e. PMs), and a trailing/rostral aggregate also including cells expressing $Cxcr7$ (i.e. dPMs, pEs). (a–d) If the initial gap between the two fragments is large enough ($\approx 2d_a$) to inhibit adhesive interactions between individuals belonging to different clusters, the leading portion stops locomotion and stretches (having only $Cxcr4$), while the trailing one preserves its directional movement (having both SDF1a receptors). Once the two fragments are close enough, they rejoin *via* adhesive interactions and primordium normal migration is restored. (e,f) In the absence of the trailing fragment, the leading cluster still arrests and stretches. (g,h) If the initial gap between the two fragments is too small ($\approx d_a$), the normal locomotion of the primordium is preserved. (Online version in colour.)

interactions between elements belonging to the different fragments. As shown in figure 6a–d, the leading cluster immediately stops locomotion and stretches, elongating in both directions along the stripe of SDF1a: all its component individuals (both at the front and at the rear area) in fact express the migratory protein $Cxcr4$ and therefore try to extend towards the chemical stripe, resulting in a net null displacement. The trailing aggregate conversely preserves its chemical-induced migration. Only the particles at its front area in fact express $Cxcr4$, while its mature rosette is formed by pE agents, which instead have the non-migratory SDF1a-receptor $Cxcr7$: such a receptor polarization allows the movement of the overall fragment. As soon as the two fragments come close enough they adhere and the normal movement of the remaining body of the primordium is resumed. This behaviour is in remarkable agreement with the corresponding empirical results described in [11]. Interestingly, the substantial stretching of the leading fragment is independent from the presence of the trailing one, as observed both experimentally and computationally via ablation of the trailing cluster, see figure 6e,f and [11], respectively. On the other hand, in [11], the arrest of the leading cluster is not observed when the gap between the two fragments is short enough. Such a situation is easily reproduced numerically by the removal of a smaller group of PM cells (i.e. of a nearly d_a-wide stripe) just close to the head of the primordium along with the deposited proto-neuromast, see figure 6g,h.
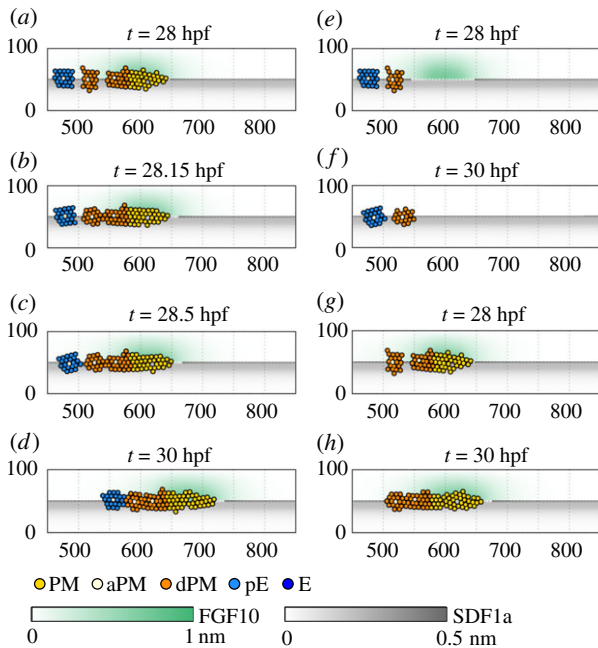
Figure 7. Numerical simulations reproducing experiments performed in [11] where the migrating primordium is divided into three fragments via laser ablation: a trailing/rostral mature rosette (including *Cxcr7*-expressing cells); a central immature rosette and a leading/caudal cluster (both having *Cxcr4*-expressing cells only). (a–d) The trailing and leading fragments arrest, while the central isolated rosette moves forward. The trailing rosette stops as it is mainly constituted by *Cxcr7*-expressing cells. The different behaviour of the central and leading fragments (both including *Cxcr4*-expressing cells only) is related to FGF10-signalling: dPM cells forming the immature rosette express *fgfr1*, which pushes them towards PM and aPM sources of FGF10. Once the central and leading clusters are close enough they aggregate and stretch, thereby allowing the reconstruction of the primordium via adhesive interactions. Normal locomotion is then restored. (e,f) In the absence of the leading fragment, both the trailing and the central isolated clusters arrest. (g,h) The absence of the trailing fragment does not affect the behaviour of the other clusters, which are still able to aggregate. The resulting cluster is however unable to move until the previously isolated central rosette undergoes partial epithelialization, thereby allowing a productive pattern of receptors *Cxcr7/Cxcr4*. (Online version in colour.)

Consistently with the corresponding experimental results, the two virtual clusters quickly adhere and the normal locomotion of the embryonic organ is preserved.

Laser ablation is also used to dissect the primordium in three fragments: a leading cluster and a central isolated immature rosette, both expressing *Cxcr4*, and a trailing aggregate characterized instead by *Cxcr7*, see again [11]. To reproduce such an *in vitro* configuration, we again let the numerical primordium to normally develop until 28 hpf: then, we isolate the second rosette within the main body of the proto-organ by removing proper groups of individuals in its surroundings, see figure 7a. The leading fragment is indeed formed by progenitor PM individuals and by a newly formed proto-neuromast, whereas the trailing portion comprises a partially epithelialized rosette (i.e. formed by pE agents). Also in this case, the deposited rosette is not considered at all. As reproduced in figure 7a–d, the trailing and the leading fragments are unable to move, whereas the isolated proto-neuromast migrates forward and quickly comes into contact with the leading cluster. In particular, the partially epithelialized proto-neuromast does not move as a consequence of the lack of the

polarized expression of SDF1a receptors (the migratory-related *Cxcr4* is in fact expressed only by the aPM that is constrained by its enhanced adhesiveness at the centre of the rosette), see figure 7b. Such a mechanistic rationale should in principle also prevent the locomotion of the isolated rosette: however, its component dPM cells have *fgfr1*, which pushes them towards FGF10-producing PM individuals located in the leading fragment. By re-adhesion, the central immature rosette and the caudal fragment then form an aggregate with inhibited SDF1a-induced directional movement: all its component particles in fact express *Cxcr4*, see figure 7c. However, its horizontal stretching allows the formation of adhesive contacts with the epithelial rostral rosette. A wild-type embryonic organ therefore somehow emerges again, with the normal inner polarization of SDF1a receptors that allows a productive directional migration, see figure 7d. The phenomenology captured by this numerical realization is close to the corresponding empirical evidence, see fig. 4 in [11]. In particular, the fact that the isolated immature central rosette moves upon FGF10 signals triggered by PM cells is clearly supported by the stopping of its locomotion in the case of removal of the leading fragment, as shown computationally in figure 7e,f and experimentally in [11]. Interestingly, in this case, the central rosette does not elongate as one may expect: the underlying reason can be found in the stabilization actuated by the aPM via its enhanced adhesiveness and FGF10 signals. On the opposite side, the presence of the trailing proto-neuromast does not affect the behaviour of the central rosette. In fact, when only the most rostral epithelialized rosette is removed (see figure 7g,h and [11]) the central and the leading fragments are still able to aggregate (as observed in figure 7a,b) but not to move, at least until the previously isolated central rosette undergoes partial epithelialization, thereby expressing *Cxcr7* proteins and allowing a productive pattern of SDF1a receptors.

Finally, for the sake of completeness, the model outcomes in figures 8 and 9 highlight how variations in the free model parameters (i.e. the adhesion/repulsion coefficients, cell chemical sensitivity and SDF1a internalization rates) affect the numerical outcomes in figures 6 and 7, respectively. In particular, we there report representative final configurations obtained in the case of decrease/increase of one of the referred free model parameters.

Too low adhesive/repulsive coefficients (e.g. a reduction of one degree of magnitude in both v_{rep}, v_{adh} and V_{adh}) result in a stretching of the fragments (or portions of fragments) constituted by PM and dPM agents, being in fact more free to move according to the detected pattern of FGF10 (dPMs only) and SDF1a (both PMs and aPMs). The fragments indeed excessively elongate along the stripe of SDF1a. Moreover, when the mature rosette comprising the dE agent is present (see figures 8a, 8c, 9a and 9b), too low interaction coefficients are not able to rebuild a unique placode and the mature rosette indeed remains almost still. In turn, the resulting fragmentation prevents the emergence of a directional locomotion. In the opposite case, too high adhesive/repulsive coefficients (e.g. a doubling of both v_{rep}, v_{adh} and V_{adh}) significantly affect only the numerical outcomes reported in figure 7e,f, see figure 9b. It in fact allows the caudal and central fragments to come close by adhesion and thus constitute a compact aggregate with dPM individuals (expressing *Cxcr4*) at its caudal edge and pE agents (having *Cxcr7*) at its rostral edge. The resulting aggregate is thus able to undergo locomotion over the stripe of SDF1a and to move towards the embryo's tail. In all the other cases, too high adhesive/repulsive
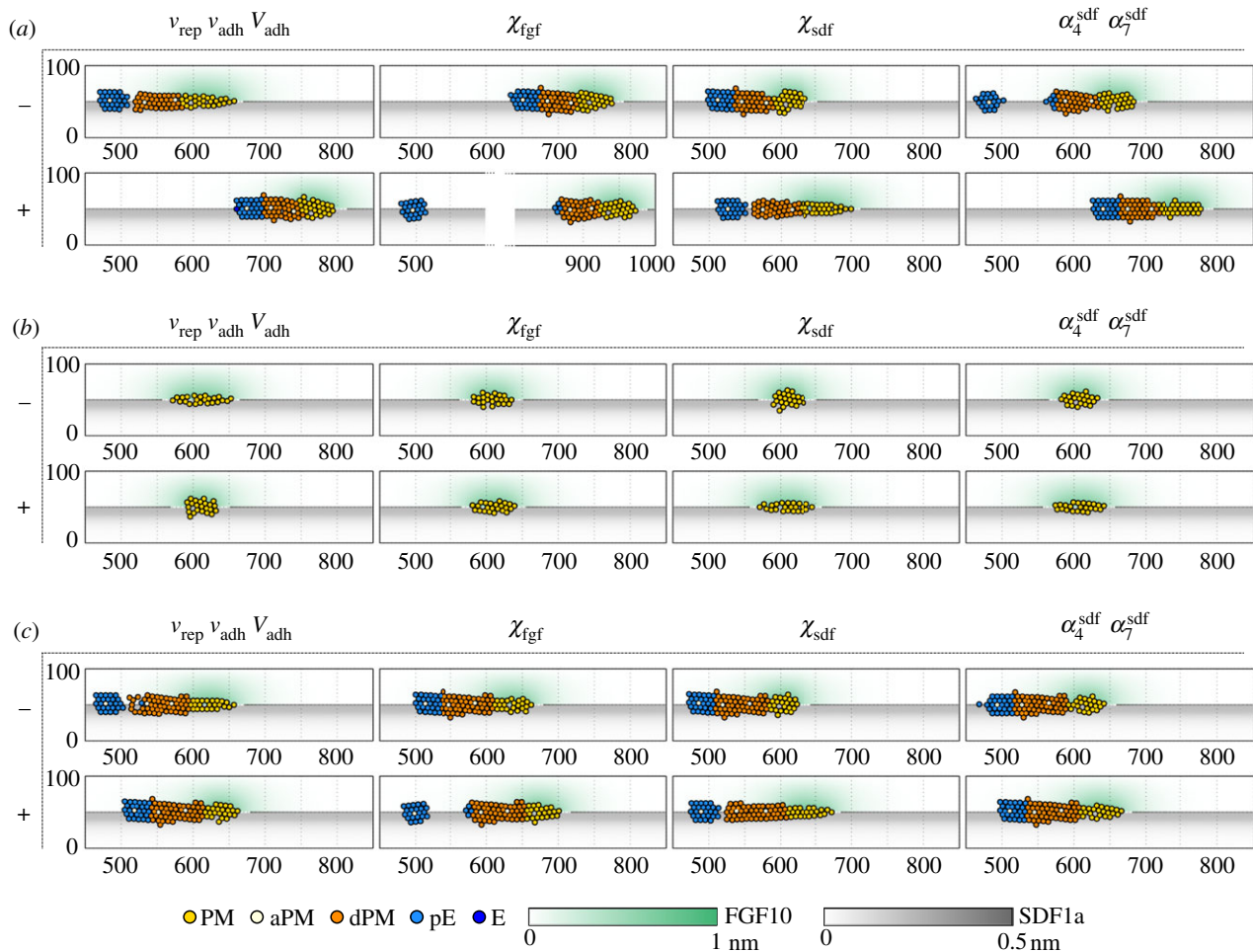
Figure 8. Dependence of the numerical outcomes in figure 6 upon decreases (−) or increases (+) of one of the free model parameters: i.e. the adhesion/repulsion coefficients (ν_{rep}, ν_{adh} and V_{adh}), cell chemical sensitivity (i.e. χ_{fgf} or χ_{sdf}) and SDF1a internalization rates (i.e. α_4^{sdf} and α_7^{sdf}). (a) Manipulations of the simulation in figure 6a–d. All panels show system configuration at $t = 30$ hpf. (b) Manipulations of the numerical test in figure 6e,f. All panels show system configuration at $t = 29$ hpf. (c) Manipulations of the numerical test in figure 6g,h. All panels show system configuration at $t = 28.5$ hpf. (Online version in colour.)

coefficients slightly affect cell dynamics by leading to a rounder configuration of the fragments.

Too low cell chemical sensitivity to FGF10 (e.g. a reduction of one degree of magnitude in χ_{fgf}) does not significatively vary the evolution of the considered systems, cf. figure 6 with figure 8, and figure 7 with figure 9. Too high cell chemical sensitivity to FGF10 (e.g. an increase of one degree of magnitude in χ_{fgf}) obviously does not change the dynamics in figures 6e,f and 7e,f (as they include either PM individuals or *fgfr1*-expressing cells only, cf. with figures 8b and 9b, respectively), but avoid the reconstruction of the primordium in all other cases. When the primordium is divided in two fragments, see figure 8a,c, the trailing fragment further separates in two portions: dPM individuals at its caudal edge indeed rapidly move towards PMs (being subjected to an increased chemoattractant cue) and detach from most rostral pEs which stay still. The resulting caudal fragment (comprising PMs, dPMs and few pEs) moves towards the embryo's tail owing to the polarized expression of SDF1a receptors, and owing to dPM agents that both chemotactically move towards and push forward PMs, in addition to drag the few pEs by adhesion. In the case of a primordium ablated in three fragments, see figure 9a,c, too high cell sensitivity to FGF10 drives dPM individuals in the caudal fragment to move towards and rapidly push forward PM individuals. As soon as the caudal fragment moves away, *fgfr1*-expressing cells in the central (and rostral) fragment slow down and arrest, being both

too far from FGF10 secreting cells, and being comprised in fragments that mainly express only one SDF1a receptor.

Too low cell chemical sensitivity to SDF1a (e.g. a reduction of one degree of magnitude in χ_{sdf}) significatively disrupts the evolution of all the considered numerical simulations. When the primordium is divided in two fragments, see figure 8a,c, the trailing portion moves forward and reaches the leading fragment owing to FGF10-dependent velocity components (driving dPM and pE cells expressing *fgfr1*) and to cell-cell adhesions. The primordium is thus rebuilt, but it presents a more compact morphology and is not able to undergo normal locomotion in the presence of too low SDF1a-related velocity components. For the same reason the leading fragment in figure 8b does not elongate as in figure 6e,f . Analogously, when the primordium is divided into three fragments, a reduction in the value of χ_{sdf} allows the fragments to rejoin in any case, see figure 9. This suggests that the aggregation of primordium fragments is mainly regulated by adhesive interactions and FGF10-signalling, which here overcome SDF1a-related velocity components. This is further confirmed by the fact that the resulting aggregate presents a more compact and rounded morphology, and that it is not able to migrate along the stripe of SDF1a even if the polarized expression of receptors *Cxcr4/Cxcr7* occurs (figure 9a,b). On the other hand, too high cell chemical sensitivity to SDF1a (e.g. an increase of one degree of magnitude in χ_{sdf}) results in an extremely stretched configuration of the fragments (or portions of fragments)
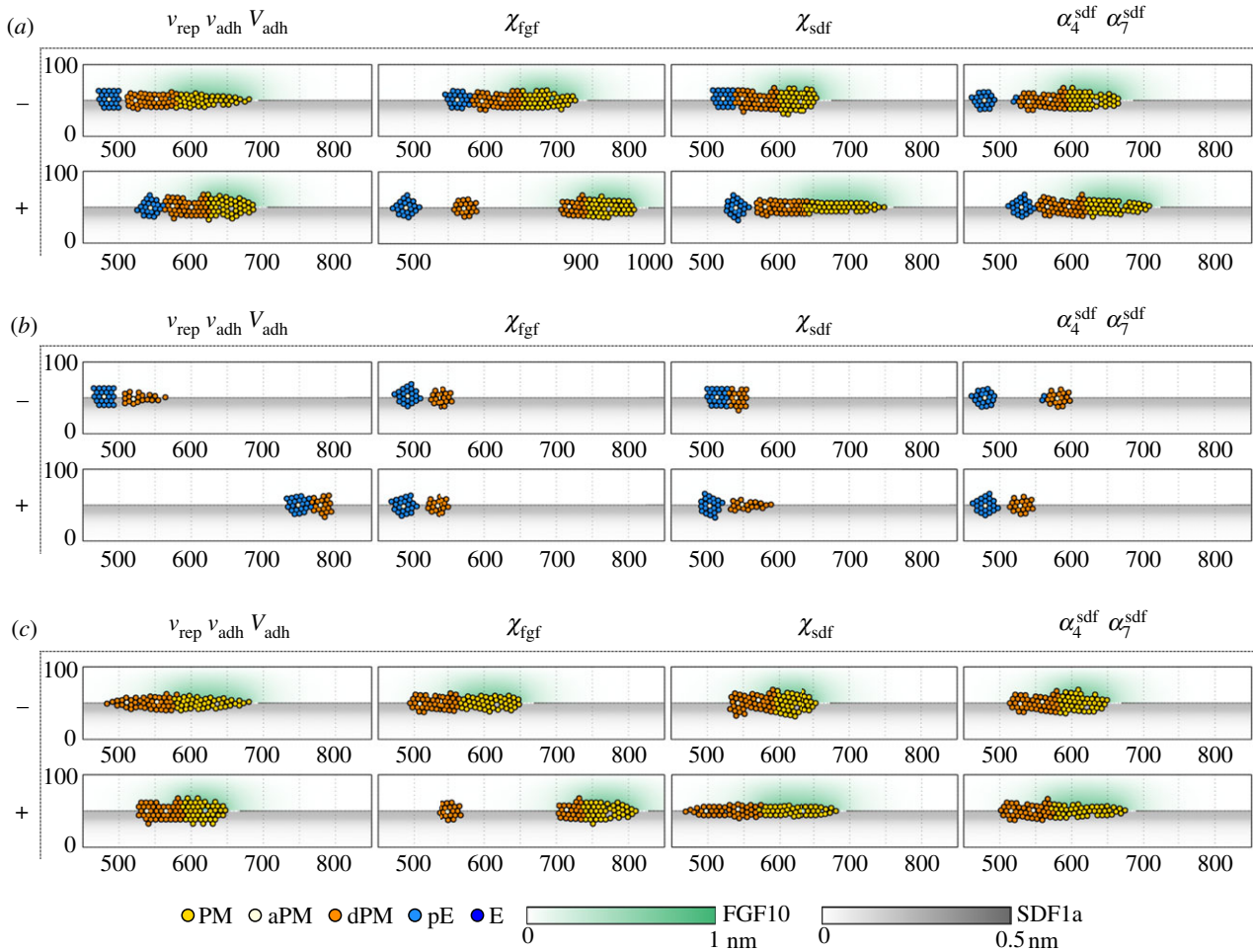
Figure 9. Dependence of the numerical outcomes in figure 7 upon decreases (−) or increases (+) of one of the free model parameters: i.e. the adhesion/repulsion coefficients (v_{rep}, v_{adh} and V_{adh}), cell chemical sensitivity (i.e. χ_{fgf} or χ_{sdf}), and SDF1a internalization rates (i.e. α_4^{sdf} and α_7^{sdf}). All panels show system configuration at $t = 30$ hpf. (a) Manipulations of the simulation in figure 7a–d. (b) Manipulations of the numerical test in figure 7e,f. (c) Manipulations of the numerical test in figure 7g,h. (Online version in colour.)

mainly constituted by *Cxcr4*-expressing cells, i.e. PMs and dPMs, see both figures 8 and 9. Moreover, in figures 8a, 8c and 9(a), too high SDF1a-related contributions drives most rostral dPM individuals to rapidly move forward as soon as pEs in the mature rosette are close enough. This therefore causes (or maintains) a minimal distance between *Cxcr7* expressing cells and agents having *Cxcr4*, that prevents the normal primordium locomotion observed in figures 6a–d, 6g,h and 9a–d, respectively.

Too low SDF1a internalization rates (e.g. a reduction of α_4^{sdf} to 0.01, which gives $\alpha_7^{sdf} = 0.1$) result in (i) a reduced elongation of the fragments (or portion of fragments) constituted by PM and dPM individuals, i.e. of the regions where cells express the migratory receptor *Cxcr4*, (ii) an abnormal disruption of the mature rosette (comprising pEs), and (iii) anomalies in fragment locomotion, see figures 8 and 9. In the case of negligible affinity of both SDF1a receptors for their ligand, the self-generated local gradient of SDF1a underlying the placode is in fact too weak with respect to adhesive/repulsive interactions and FGF10-related velocity components. Conversely, too high SDF1a internalization rates (e.g. an increase of α_4^{sdf} to 0.09, which gives $\alpha_7^{sdf} = 0.9$) do not strongly change the evolution of the numerical simulations in figures 6 and 7. We can only note that the regions constituted by *Cxcr4*-expressing cells result more stretched as in the case of too high cell sensitivity to SDF1a.

5. Conclusion

The embryonic formation of the zebrafish PLL is a phenomenon of particular interest in developmental biology. It in fact allows us to shed lights on several mechanisms and processes underlying chemically induced collective movement and organization. PLL morphogenesis involves the migration of a primordium formed by epithelial cells with mesenchymal characteristics, which undergo cyclical phenotypic differentiations resulting in the assembly and deposition of rosette-like structures (i.e. progenitor of neuromast sensory organs).

In the present work, this phenomenon has been approached from a modelling perspective by proposing a discrete model with hybrid characteristics. Cells were represented by interacting particles moving according to first-order integro-differential equations; diffusive molecular substances by continuous concentrations evolving following RD equations; and chemical receptors by Boolean variables. In particular, in order to take into account the extension of a cell body, the individuals were also characterized by a range of influence and perception. Non-local interaction terms then reproduce cell-cell direct interactions (adhesion/repulsion), while integral velocity components implement FGF10- and SDF1a-related dynamics. Specifically, proper weight functions were included in the integrals in order to take into account that a local fraction of the chemical

substances can be temporarily unavailable for a given cell as it may be actually sequestered by surrounding individuals. Finally, the proposed approach is also equipped by proper rules for cell duplication and phenotypic transitions.

With respect to the models already present in literature (and summarized in §2b), an innovative aspect of the proposed approach is to include both (i) SDF1a and FGF10 signalling driving primordium locomotion; (ii) SDF1a-receptors Cxcr4 and Cxcr7; (iii) the formation, maturation and deposition of proto-neuromasts; and (iv) cell proliferation. As already commented in §2a, for the sake of simplicity, Fgf/Wnt signalling, as well as Delta-Notch pathways, involved in rosette formation, were not included in this work. In fact, we have here opted for a simplified characterization of both cell phenotypes and relative pseudo-mesenchymal-to-epithelial transitions regulating rosette formation which allow us to neglect complex processes occurring at subcellular scales. It in fact allows us to focus on the dynamic expression of different receptors within the primordium and the consequent onset of its directional locomotion. In more detail, the underlying hypothesis of the proposed approach is that the progressive organization of PMs into rosette-like clusters regulates both the polarization of receptors Cxcr4/Cxcr7 along the primordium, and the subdivision of the placode in a leading portion of PM cell secreting FGF10 and a trailing portion mainly comprising cells expressing the receptor fgfr1. Another relevant aspect of the proposed approach with respect to previous mathematical works is that, according to experimental observations in, among others, [5,8,10], it takes into account that the expression of SDF1a-receptor Cxcr4 is not limited to the leading PM cells secreting FGF10 only.

The numerical outcomes reported in the present work have shown that the proposed model is able to reproduce empirical evidences regarding both the physiological development of the proto-organ and selected experimental manipulation involving laser ablation. Moreover, system behaviours observed upon variations in the free model parameters highlight that the proposed implementation of SDF1a- and FGF10-related velocity contributions are able to capture that the directional locomotion of the primordium is actually triggered by the polarized expression and activity of the receptors Cxcr4/Cxcr7, and sustained by FGF-related contributions and adhesive interactions.

It has been further observed in silico that FGF-signalling and cell-cell direct interactions, as well as altered levels of activity of SDF1a-related receptors, differently affect the initial typical elongation of the primordium. On the one hand, too low interactions and FGF-signalling leads to an extremely stretched placode, while too low activity of SDF1a related receptors results in an extremely compacted primordium. It would be highly interesting and useful to compare these numerical outcomes with experimental results. It would in

fact either validate the proposed model and the underlying assumptions, or (hopefully) suggest which refinements are necessary to improve its realism and predictive potential.

Of course, there are still several aspects that require further investigation to completely understand and control the processes underlying the development of zebrafish PLL. One of these aspects is the mechanisms regulating the selection of PM cells that will undergo activation thereby triggering rosette formation. In this respect, it has been observed that FGF-signalling pathways affect not only the dynamics of fgfr1-expressing cells, but they are also included in both cell phenotypic activation (as inhibition of FGFs also results in the disaggregation of immature rosettes, i.e. with dPMs) and, possibly, in cell duplication. It would be therefore coherent to include also Wnt/Fgf signalling pathways and Delta-Notch pathways involved in cell phenotypic differentiations. Moreover, deepening experimental investigations of the mechanisms establishing the exact timing and pattern of cell activation and rosette deposition would be relevant as well. In this context, another aspect that may be interesting to study is whether the overall growth of the embryo (whose length goes from 1.4 mm at t_0 to about 3 mm at t_F, according to ZFIN, see https://zfin.org/zf_info/zfbook/stages/), as well as the development of other organs, affect or even regulate the normal evolution of the PLL. An extension of the model into a 3D domain would be therefore recommended.

In this respect, it is worth noting that the extension of the model to a 3D domain is not trivial (but not impossible). Given a spatial domain $\Omega \subset \mathbb{R}^3$ and the stripe $\mathcal{H} \subset \Omega$, where the stromal-derived factor is produced, it requires a careful reassessment of several aspects, e.g. the cell range of influence and perception, the non-local cell-cell and cell-chemicals interaction terms. From a biological point of view, in a 3D context, we could further enrich the model by including the fact that, during migration, leading cells are relatively flat with respect to trailing cells. The latter, in fact, become taller because they constrict at their apical ends to acquire apical-basal polarity and reorganize into epithelial rosettes (a process that from a 2D point of view is obviously neglected).

References

1. Ghysen A, Dambly-Chaudière C. 2004 Development of the zebrafish lateral line. Curr. Opin. Neurobiol. 14, 67–73. (doi:10.1016/j.conb.2004.01.012)

2. Stone LS. 1937 Further experimental studies of the development of lateral-line sense organs in amphibians observed in living and vitalstained preparations. J. Comp. Neurol. 68, 83–115. (doi:10.1002/cne.900680105)

3. Durdu S, Iskar M, Revenu C, Schieber N, Kunze A, Bork P, Schwab Y, Gilmour D. 2014 Luminal signalling links cell communication to tissue architecture during organogenesis. Nature 515, 120–124. (doi:10.1038/nature13852)

4. Keller ET, Murtha JM. 2004 The use of mature zebrafish (Danio rerio) as a model for human aging and disease. Comp. Biochem. Physiol. C Toxicol. Phermacol. 138, 335–341. (doi:10.1016/j.cca.2004.04.001)

5. Nechiporuk A, Raible DW. 2008 FGF-dependent mechanosensory organ patterning in zebrafish. *Science* **320**, 1774–1777. (doi:10.1126/science.1156547)

6. Streisinger G, Walker C, Dower N, Knauber D, Singer F. 1981 Production of clones of homozygous diploid zebra fish (*Brachydanio rerio*). *Nature* **291**, 293–296. (doi:10.1038/291293a0)

7. Kimmel CB, Ballard WW, Kimmel SR, Ullmann B, Schilling TF. 1995 Stages of embryonic development of the zebrafish. *Dev. Dyn.* **203**, 253–310. (doi:10.1002/aja.1002030302)

8. Aman A, Piotrowski T. 2008 Wnt/β-catenin and FGF signaling control collective cell migration by restricting chemokine receptor expression. *Dev. Cell* **15**, 749–761. (doi:10.1016/j.devcel.2008.10.002)

9. Aman A, Piotrowski T. 2009 Multiple signaling interactions coordinate collective cell migration of the posterior lateral line primordium. *Cell Adh. Migr.* **3**, 365–368. (doi:10.4161/cam.3.4.9548)

10. Aman A, Nguyen M, Piotrowski T. 2011 Wnt/β-catenin dependent cell proliferation underlies segmented lateral line morphogenesis. *Dev. Cell* **349**, 470–482. (doi:10.1016/j.ydbio.2010.10.022)

11. Dalle Nogare D, Somers K, Rao S, Matsuda M, Reichman-Fried M, Raz E, Chitnis AB. 2014 Leading and trailing cells cooperate in collective migration of the zebrafish posterior lateral line primordium. *Development* **141**, 3188–3196. (doi:10.1242/dev.106690)

12. Dalle Nogare D, Chitnis AB. 2017 A framework for understanding morphogenesis and migration of the zebrafish posterior lateral line primordium. *Mech. Dev.* **148**, 69–78. (doi:10.1016/j.mod.2017.04.005)

13. Dambly-Chaudière C, Cubedo N, Ghysen A. 2007 Control of cell migration in the development of the posterior lateral line: antagonistic interactions between the chemokine receptors CXCR4 and CXCR7/RDC1. *BMC Dev. Biol.* **7**, 23. (doi:10.1186/1471-213X-7-23)

14. Donà E, Barry JD, Valentin G, Quirin C, Khmelinskii A, Kunze A, Durdu S, Newton LR, Fernandez-Minan A, Huber W, Knop M, Gilmour D. 2013 Directional tissue migration through a self-generated chemokine gradient. *Nature* **503**, 285–289. (doi:10.1038/nature12635)

15. Gompel N, Cubedo N, Thisse C, Thisse B, Dambly-Chaudière C, Ghysen A. 2001 Pattern formation in the lateral line of zebrafish. *Mech. Dev.* **105**, 69–77. (doi:10.1016/S0925-4773(01)00382-3)

16. Knutsdottir H, Zmurchok C, Bhaskar D, Palsson E, Dalle Nogare D, Chitnis AB, Edelstein-Keshet L. 2017 Polarization and migration in the zebrafish posterior lateral line system. *PLoS Comput. Biol.* **13**, e1005451. (doi:10.1371/journal.pcbi.1005451)

17. Lecaudey V, Cakan-Akdogan G, Norton WH, Gilmour D. 2008 Dynamic FGF signaling couples morphogenesis and migration in the zebrafish lateral line primordium. *Development* **135**, 2695–2705. (doi:10.1242/dev.025981)

18. Metcalfe WK. 1985 Sensory neuron growth cones comigrate with posterior lateral line primordial cells in zebrafish. *J. Comp. Neurol.* **238**, 218–224. (doi:10.1002/cne.902380208)

19. Valentin G, Haas P, Gilmour D. 2007 The chemokine SDF1a coordinates tissue migration through the spatially restricted activation of Cxcr7 and Cxcr4b. *Curr. Biol.* **17**, 1026–1031. (doi:10.1016/j.cub.2007.05.020)

20. Allena R, Maini P. 2014 Reaction-diffusion finite element model of lateral line primordium migration to explore cell leadership. *Bull. Math. Biol.* **76**, 3028–3050. (doi:10.1007/s11538-014-0043-7)

21. Chitnis AB, Dalle Nogare D. 2011 A computational model reveals the remarkable patterning potential of the Wnt-FGF gene regulatory network in the posterior latelal line primordium. *Dev. Biol.* **356**, 111. (doi:10.1016/j.ydbio.2011.05.039)

22. Di Costanzo E, Natalini R, Preziosi L. 2014 A hybrid mathematical model for self-organizing cell migration in the zebrafish lateral line. *J. Math. Biol.* **71**, 171–214. (doi:10.1007/s00285-014-0812-9)

23. Streichan SJ, Valentin G, Gilmour D, Hufnagel L. 2011 Collective cell migration guided by dynamically maintained gradients. *Phys. Biol.* **8**, 045004. (doi:10.1088/1478-3975/8/4/045004)

24. Carrillo JA, Colombi A, Scianna M. 2018 Adhesion and volume constraints via nonlocal interactions determine cell organisation and migration profiles. *J. Theor. Biol.* **445**, 75–91. (doi:10.1016/j.jtbi.2018.02.022)

25. Drasdo D. 2003 On selected individual-based approaches to the dynamics in multicellular systems. In *Polymer and cell dynamics. Multiscale modeling and numerical simulations* (eds W Alt, M Chaplain, M Griebel, J Lenz), pp. 169–203. Basel, Switzerland: Birkhäuser.

26. Scianna M, Preziosi L. 2012 Multiscale developments of the cellular Potts model. *Multiscale Model. Simul.* **10**, 342–382. (doi:10.1137/100812951)

27. David N, Sapède D, Saint-Etienne L, Thisse C, Thisse B, Dambly-Chaudière C, Rosa FM, Ghysen A. 2002 Molecular basis of cell migration in the fish lateral line: role of the chemokine receptor CXCR4 and of its ligand, SDF1. *Proc. Natl Acad. Sci. USA* **99**, 16 297–16 302. (doi:10.1073/pnas.252339399)

28. Haas P, Gilmour D. 2006 Chemokine signaling mediates self-organizing tissue migration in the zebrafish lateral line. *Dev. Cell* **10**, 673–680. (doi:10.1016/j.devcel.2006.02.019)

29. Cañizo JA, Carrillo JA, Patacchini FS. 2015 Existence of compactly supported global minimisers for the interaction energy. *Arch. Ration. Mech. Anal.* **217**, 1197–1217. (doi:10.1007/s00205-015-0852-3)

30. Cañizo JA, Patacchini FS. 2018 Discrete minimisers are close to continuum minimisers for the interaction energy. *Calc. Var. Partial Differ. Equ.* **57**, 24. (doi:10.1007/s00526-017-1289-3)

31. Gilmour D, Haas P, Lecaudey V, Streichan SJ, Valentin G. 2009 S20-05 Dissecting the role of extrinsic and intrinsic cues in coordinating collective cell migration. *Mech. Dev.* **126**, S21. (doi:10.1016/j.mod.2009.06.1006)